ChemComm

COMMUNICATION

View Article Online
View Journal

Check for updates

Cite this: DOI: 10.1039/d6cc00986g

Received 17th February 2026,
Accepted 10th April 2026

DOI: 10.1039/d6cc00986g

rsc.li/chemcomm

High-performance, acid-durable nonprecious ternary alloy cathode *via* Zn dealloying for proton exchange membrane water electrolysis

Chan Hee Lee, † Kyeong-Rim Yeo † and Soo-Kil Kim *

We present a nonprecious NiMo-based cathode with high activity and durability for proton exchange membrane water electrolysis, achieved *via* selective Zn dealloying and subsequent thermal annealing. This synergistic strategy simultaneously increases the electrochemically active surface area, achieving 1.897 A cm^{-2} at 2.0 V_{cell}, and ensures structural stability in acidic media.

The intermittency of renewable energy sources challenges grid stability, driving the need for efficient energy storage systems (ESSs). Hydrogen-based storage is promising due to its zero emissions and suitability for long-term, large-scale use,[1] making renewable-powered water electrolysis a key route for green hydrogen production.[2,3]

Proton exchange membrane water electrolysis (PEMWE) enables high current density, high-purity hydrogen, and compact design compared with alkaline systems,[3,4] but its acidic operation requires costly precious metal cathodes (*e.g.*, Pt, Ru), limiting scalability.[5] Strategies such as alloying,[6,7] single atom catalysts,[8,9] and template-assisted synthesis[10,11] have been explored, with electrochemical dealloying emerging as an effective approach.[11–13] Electrochemical dealloying selectively removes less noble components to increase the electrochemically active surface area (ECSA) of the catalyst.[14] However, for practical PEMWE, developing nonprecious metal electrodes with comparable performance remains essential. Despite efforts including morphology regulation,[15,16] alloying,[16–18] and heterostructure engineering,[19,20] dealloying studies on noble-metal-free alloys are limited, mainly due to the small differences in standard reduction potentials among transition metals, compared with those between precious and transition metals, making selective dealloying more challenging. NiMo-based alloys are reported to be highly efficient hydrogen evolution reaction (HER) catalysts. Recent studies have extended this system to multicomponent alloys, such as NiMoZn[18] and CuNiMo,[17] mainly investigating alloying effects. In particular, the incorporation of a small amount of Zn (1–3 at%) into NiMo was reported to enhance HER activity, achieving a low overpotential of 40 mV at −20 mA cm^{-2}.[18] Furthermore, we previously reported that Mn incorporation into NiMo (NiMoMn) improves intrinsic HER activity and acid durability *via* electronic structure modulation.[21] However, such alloying strategies have limited impact on increasing ECSA. Here, we instead employ Zn as a sacrificial component for selective dealloying to create a porous Ni–Mo framework. To address the durability issue of dealloyed catalyst, post-annealing was employed to improve catalyst stability. Beyond half-cell tests, single-cell evaluations confirmed the catalyst's performance and long-term stability in PEMWE, demonstrating its practical applicability.

Fig. 1 shows the field emission scanning electron microscopy (FESEM) images and energy dispersive X-ray spectroscopy (EDS) mapping of the catalysts at different processing stages. In Fig. 1a, the pristine $Ni_{81.6}Mo_{2.4}Zn_{16.0}$ (P-$Ni_{81.6}Mo_{2.4}Zn_{16.0}$) catalyst forms a continuous film composed of aggregated spherical particles covering the carbon fibers. At higher magnification, cauliflower-like hierarchical structures with locally vertical particle growth were observed, imparting a roughened surface morphology. EDS mapping confirmed a homogeneous spatial distribution of Ni, Mo, and Zn, consistent with the bulk composition. Following electrochemical dealloying (Fig. 1b), D-$Ni_{85.9}Mo_{3.3}Zn_{10.8}$ possesses a partially reduced film structure and an increased fraction of vertically grown spherical features. This morphological evolution reflects selective Zn dissolution, leading to

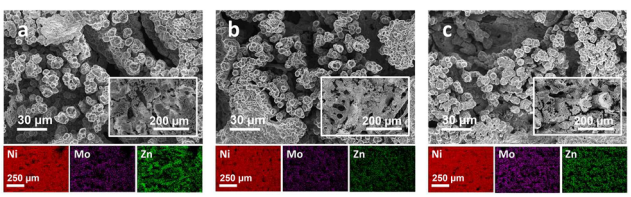


Fig. 1 FESEM and EDS mapping images of (a) P-$Ni_{81.6}Mo_{2.4}Zn_{16.0}$, (b) D-$Ni_{85.9}Mo_{3.3}Zn_{10.8}$, and (c) HD-$Ni_{86.7}Mo_{3.2}Zn_{10.1}$ species.

School of Integrative Engineering, Chung-Ang University, 84 Heukseok-ro, Dongjak-gu, Seoul 06974, Republic of Korea. E-mail: sookilkim@cau.ac.kr
† Contributed equally.

Open Access Article. Published on 17 April 2026. Downloaded on 4/28/2026 2:08:19 AM.
This article is licensed under a Creative Commons Attribution-NonCommercial 3.0 Unported Licence.

Open Access Article. Published on 17 April 2026. Downloaded on 4/28/2026 2:08:19 AM.
This article is licensed under a Creative Commons Attribution-NonCommercial 3.0 Unported Licence.

surface roughening and the formation of a more porous, ligament-like structure. Correspondingly, the bulk Zn content decreased from 16.0 to 10.8 at%, whereas Ni and Mo remain uniformly distributed although Zn uniformity was slightly reduced. As shown in Fig. 1c, the heat-treated D-$Ni_{86.7}Mo_{3.2}Zn_{10.1}$ (HD-$Ni_{86.7}Mo_{3.2}Zn_{10.1}$) catalyst maintains the porous morphology of the dealloyed sample with minor surface coarsening, suggesting improved structural stability. The EDS results indicate that heat treatment did not significantly alter the overall elemental distribution.

The XRD patterns (Fig. S1) show characteristic peaks of carbon paper at 42.46°, 43.02°, 44.67°, 47.37°, and 54.8° (JCPDS #26-1080). For Ni_{100}, the peaks of the (111) and (200) planes were observed at 44.5° and 51.8°, respectively (JCPDS #04-0850). For Zn_{100}, the peaks associated with the (002), (110), and (101) planes of the hexagonal close-packed structure were observed at 36.3°, 38.9°, and 43.2°, respectively (JCPDS #04-0831). In $Ni_{92.7}Mo_{7.3}$, the Ni (111) peak slightly shifted to lower angles with reduced intensity, indicating lattice expansion due to alloying with Mo atoms, which have a larger atomic radius than Ni.[17] The amorphous or nanocrystalline structure of the Ni alloy containing Mo is characterized by a poorly developed Ni lattice.[22–24] With Zn alloying, P-$Ni_{81.6}Mo_{2.4}Zn_{16.0}$ exhibits a further slight shift to lower angle owing to the larger atomic size of Zn. After dealloying, D-$Ni_{85.9}Mo_{3.3}Zn_{10.8}$, shows a shift to higher angle, consistent with Zn removal. Notably, HD-$Ni_{86.7}Mo_{3.2}Zn_{10.1}$ displays significantly enhanced Ni (111) and (200) peak intensities after annealing at 400 °C for 2 h in a 4% H_2/Ar atmosphere, indicating improved crystallinity.

To investigate the surface composition, electronic structure, and oxidation states of the samples, X-ray photoelectron spectroscopy (XPS) was performed (Fig. 2). Fig. 2a exhibits Ni $2p_{3/2}$ spectra. For Ni_{100}, peaks corresponding to Ni^0, NiO, and $Ni(OH)_2$ were observed at 852.1, 853.2, and 855.6 eV, respectively. For $Ni_{92.7}Mo_{7.3}$, these peaks were observed at 852.16, 853.26, and 855.66 eV, with the metallic Ni^0 fraction increasing from 35.6% to 46.35% and the NiO and $Ni(OH)_2$ fractions decreasing from 15.99% and 28.38% to 13.72% and 19.84%, respectively.[17] This shift is attributed to electron transfer from Mo to Ni due to their electronegativity difference. Compared to the binary NiMo sample, the P-$Ni_{81.6}Mo_{2.4}Zn_{16.0}$ exhibited increased fraction of NiO and $Ni(OH)_2$ species. Although Zn has a lower electronegativity than Ni, its incorporation alters the local electronic environment and structural order, leading to reduced local coordination of Ni or weakening of Ni–Mo metallic networks. Similar trends have been reported for binding energy changes following Zn addition.[18,25] The strong oxygen affinity of Zn further promotes interfacial oxidation, rendering surface Ni sites more susceptible to oxidation and hydroxylation. Following electrochemical dealloying, D-$Ni_{85.9}Mo_{3.3}Zn_{10.8}$ exhibited an even higher concentration of oxidized Ni species due to selective Zn dissolution, which generated defect-rich, under-coordinated Ni sites prone to oxidation. Subsequent heat treatment in a reducing 4% H_2/Ar atmosphere yielded HD-$Ni_{86.7}Mo_{3.2}Zn_{10.1}$ with partial recovery of metallic Ni, indicating defect annealing and improved metallic bonding. The coexistence

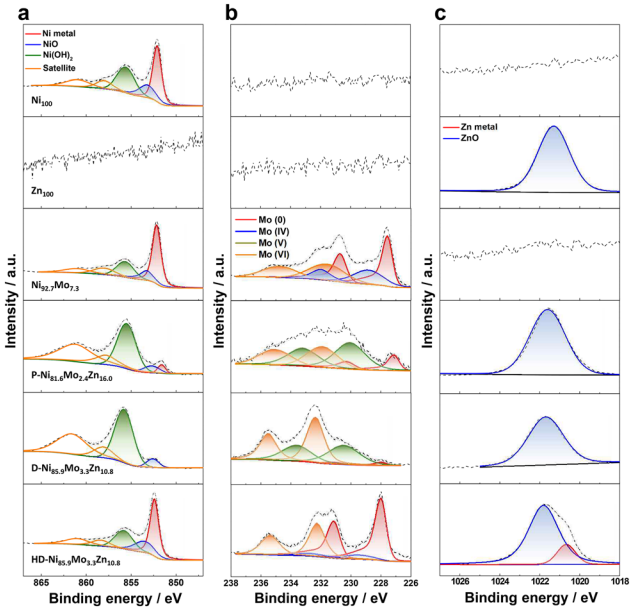


Fig. 2 XPS spectra of (a) Ni $2p_{3/2}$, (b) Mo $3d_{5/2}$, and (c) Zn $2p_{3/2}$ components of Ni_{100}, Zn_{100}, $Ni_{92.7}Mo_{7.3}$, P-$Ni_{81.6}Mo_{2.4}Zn_{16.0}$, D-$Ni_{85.9}Mo_{3.3}Zn_{10.8}$, and HD-$Ni_{86.7}Mo_{3.2}Zn_{10.1}$ species.

of metallic Ni and NiO_x species is expected to create favorable interfacial sites for proton adsorption, enhancing acidic HER activity.

Fig. 2b shows the Mo $3d_{5/2}$ peaks of the catalysts. For $Ni_{92.7}Mo_{7.3}$, Mo(0), Mo(IV), and Mo(VI) species were observed at 227.6–230.75, 228.65–231.8, and 232.35–235.2 eV, respectively. In Zn-containing P-$Ni_{81.6}$ $Mo_{2.4}Zn_{16.0}$, the Mo(0) fraction decreased from 47.10% to 16.00%, indicating enhanced surface oxidation compared to the binary alloy. Upon electrochemical dealloying, D-$Ni_{85.9}Mo_{3.3}Zn_{10.8}$, showed a further reduction of Mo(0) to 3.56%, reflecting the generation of defect-rich Mo sites due to selective Zn dissolution. After heat treatment, HD-$Ni_{86.7}Mo_{3.2}Zn_{10.1}$ exhibited a substantial recovery of metallic Mo(0) (60.40%), suggesting defect annealing and reconstruction of the Ni–Mo framework. These trends closely mirror those observed in the Ni $2p_{3/2}$ spectra, supporting the structural and electronic evolution induced by Zn incorporation, dealloying, and subsequent heat treatment.

Fig. 2c shows the Zn $2p_{3/2}$ spectra. In P-$Ni_{81.6}Mo_{2.4}Zn_{16.0}$, Zn is mainly oxidized due to its strong oxygen affinity. Upon dealloying, the Zn signal decreased in D-$Ni_{85.9}Mo_{3.3}Zn_{10.8}$, confirming selective dissolution. Following annealing, HD-$Ni_{86.7}Mo_{3.2}Zn_{10.1}$ shows a weak residual Zn signal with a minor new peak, indicating Zn remains in a segregated state rather than reintegrating into the metallic framework. These results suggest Zn primarily acts as a sacrificial component that induces structural and electronic modulation of the Ni–Mo framework, rather than a direct active species for the HER.

To verify the effect of dealloying, the surface compositions of P-$Ni_{81.6}Mo_{2.4}Zn_{16.0}$ and D-$Ni_{85.9}Mo_{3.3}Zn_{10.8}$ obtained by XPS are compared with their bulk compositions determined by EDS analysis (Table S1). For P-$Ni_{81.6}Mo_{2.4}Zn_{16.0}$, the bulk compositions

This journal is © The Royal Society of Chemistry 2026

Open Access Article. Published on 17 April 2026. Downloaded on 4/28/2026 2:08:19 AM.
This article is licensed under a Creative Commons Attribution-NonCommercial 3.0 Unported Licence.

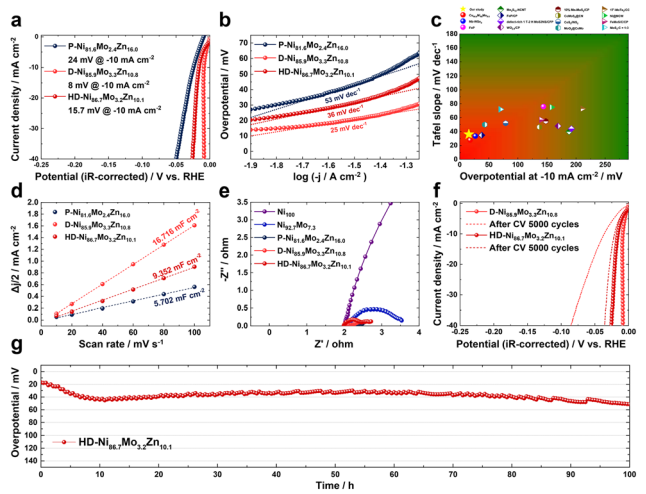


Fig. 3 (a) HER polarization curves measured with a scan rate of 1 mV s^{-1} (*iR*-compensated). (b) HER Tafel plots obtained from (a). (c) HER performance of HD-$Ni_{86.7}Mo_{3.2}Zn_{10.1}$ and reported nonprecious catalysts. (d) Measurement of electrochemical double-layer capacitance (C_{dl}) in 1 M NaOH. (e) Nyquist plots. (f) HER polarization results for 1st and 5000th curves obtained for D-$Ni_{85.9}Mo_{3.3}Zn_{10.8}$ and HD-$Ni_{86.7}Mo_{3.2}Zn_{10.1}$. (g) Chronopotentiometry result obtained over 100 h at −10 mA cm^{-2} for HD-$Ni_{86.7}Mo_{3.2}Zn_{10.1}$.

(Ni 81.6%, Mo 2.4%, Zn 16.0%) differed markedly from the XPS results (Ni 35.0%, Mo 4.0%, Zn 61.0%), indicating a pronounced surface enrichment of Zn. This enrichment could be attributed to the surface segregation, as Zn exhibits a lower segregation energy (E_{seg}) of −0.503 eV than Mo (0.394 eV) on the Ni(111), making Zn thermodynamically more stable at the surface.[26] In contrast, for D-$Ni_{85.9}Mo_{3.3}Zn_{10.8}$, although the bulk Zn content decreased modestly from 16.0% to 10.8%, the surface Zn concentration dropped dramatically from 60.96% to 17.71%, clearly demonstrating the selective dissolution of Zn during electrochemical dealloying.

Fig. 3 exhibits the HER activity and electrochemical characterization of the catalysts. As shown in Fig. 3a, P-$Ni_{81.6}Mo_{2.4}Zn_{16.0}$ exhibited an overpotential of 24 mV at −10 mA cm^{-2}, but shows an oxidation current at potentials more positive than −10 mV, indicating Zn dissolution. In comparison, D-$Ni_{85.9}Mo_{3.3}Zn_{10.8}$ showed a significantly reduced overpotential of 8 mV, whereas HD-$Ni_{86.7}Mo_{3.2}Zn_{10.1}$ exhibited a slightly higher overpotential of 15.7 mV. For accurate HER comparison, performance was benchmarked against commercial Pt/C (Table S2). HD-$Ni_{86.7}Mo_{3.2}Zn_{10.1}$ exhibited 28 mV overpotential at −50 mA cm^{-2}, nearly identical to Pt/C (difference of 0.5 mV), demonstrating excellent performance. The XPS results revealed that dealloying significantlys increased the fraction of oxidized and under-coordinated Ni and Mo species, indicative of defect-rich surface sites, correlating with the superior HER activity of D-$Ni_{85.9}Mo_{3.3}Zn_{10.8}$. Subsequent heat treatment partially restored metallic Ni and Mo, resulting in a slight decrease in activity while maintaining improved performance. In contrast, P-$Ni_{81.6}Mo_{2.4}Zn_{16.0}$ exhibited a Zn-perturbed Ni–Mo surface with increased Ni oxidation and fewer defect-related active sites, leading to comparatively lower HER activity.

Fig. 3b presents Tafel plots calculated from the HER performance curves in Fig. 3a. P-$Ni_{81.6}Mo_{2.4}Zn_{16.0}$ exhibited a Tafel slope of 53 mV dec^{-1}, indicating that the Heyrovsky step was the rate-determining step. In contrast, D-$Ni_{85.9}Mo_{3.3}Zn_{10.8}$ exhibited a lower Tafel slope of 25 mV dec^{-1}, indicating a Volmer–Tafel mechanism. HD-$Ni_{86.7}Mo_{3.2}Zn_{10.1}$ exhibited a slightly higher Tafel slope of 36 mV dec^{-1} than D-$Ni_{85.9}Mo_{3.3}Zn_{10.8}$, implying a shift in the rate-determining step consistent with the Volmer–Heyrovsky mechanism. Compared with reported nonprecious catalysts (Fig. 3c and Table S3), HD-$Ni_{86.7}Mo_{3.2}Zn_{10.1}$ demonstrates superior activity with lower overpotential and faster reaction kinetics.

Fig. 3d shows the ECSA of P-$Ni_{81.6}Mo_{2.4}Zn_{16.0}$, D-$Ni_{85.9}Mo_{3.3}Zn_{10.8}$, and HD-$Ni_{86.7}Mo_{3.2}Zn_{10.1}$, obtained from the electrochemical double-layer capacitance (C_{dl}) derived from linear sweep voltammetry (LSV) measurements at various scan rates (Fig. S2). P-$Ni_{81.6}Mo_{2.4}Zn_{16.0}$ exhibited a C_{dl} value of 5.702 mF cm^{-2}, whereas D-$Ni_{85.9}Mo_{3.3}Zn_{10.8}$ exhibited higher C_{dl} of 16.716 mF cm^{-2}, confirming the generation of abundant active sites upon dealloying. In contrast, HD-$Ni_{86.7}Mo_{3.2}Zn_{10.1}$ exhibited a lower C_{dl} value of 9.352 mF cm^{-2}, suggesting a partial loss of ECSA after heat treatment. To compare the intrinsic catalytic activity, the HER polarization curves in Fig. 3a were normalized to the roughness factor (Fig. S3). The resulting trends are consistent with those observed in the HER polarization curves.

Fig. 3e shows the Nyquist plots of the catalysts. The charge transfer resistance decreased in the order of Ni_{100} > $Ni_{94.6}Mo_{5.4}$ > P-$Ni_{81.6}Mo_{2.4}Zn_{16.0}$ > HD-$Ni_{86.7}Mo_{3.2}Zn_{10.1}$ > D-$Ni_{85.9}Mo_{3.3}Zn_{10.8}$. This observation is consistent with the XPS and HER performance evaluation results. Although heat treatment partially restores metallic states and improves conductivity, the concomitant reduction in defect density leads to a higher charge transfer resistance than that of the dealloyed catalyst.

Fig. 3f shows the accelerated degradation test (ADT) results to evaluate the durability of the catalysts. The ADT was performed over 5000 CV cycles between −0.2 to 0.05 V_{RHE}. D-$Ni_{85.9}Mo_{3.3}Zn_{10.8}$ initially showed an overpotential of 8 mV at −10 mA cm^{-2}. However, its performance significantly degraded after 5000 cycles, with an overpotential increase of 28 mV (from 8 to 36 mV), indicating limited durability. In contrast, HD-$Ni_{86.7}Mo_{3.2}Zn_{10.1}$ showed excellent durability, with only a 5 mV increase in overpotential after ADT. To probe ADT-induced changes, FESEM was conducted on D-$Ni_{85.9}Mo_{3.3}Zn_{10.8}$ and HD-$Ni_{86.7}Mo_{3.2}Zn_{10.1}$ (Fig. S4). The D-$Ni_{85.9}Mo_{3.3}Zn_{10.8}$ layer was largely peeled from carbon fibers, whereas HD-$Ni_{86.7}Mo_{3.2}Zn_{10.1}$ retained its morphology with only partial delamination, consistent with its superior electrochemical stability. While defects from Zn dealloying provide HER active sites, they also act as dissolution pathways in acidic media, unlike in alkaline conditions where stable passivation can form.[27] As shown in Fig. S1, annealing increases crystallinity and reduces defects, suppressing corrosion. The resulting lattice acts as a barrier to metal leaching, explaining the excellent long-term stability of HD-$Ni_{86.7}Mo_{3.2}Zn_{10.1}$.

Open Access Article. Published on 17 April 2026. Downloaded on 4/28/2026 2:08:19 AM.
This article is licensed under a Creative Commons Attribution-NonCommercial 3.0 Unported Licence.

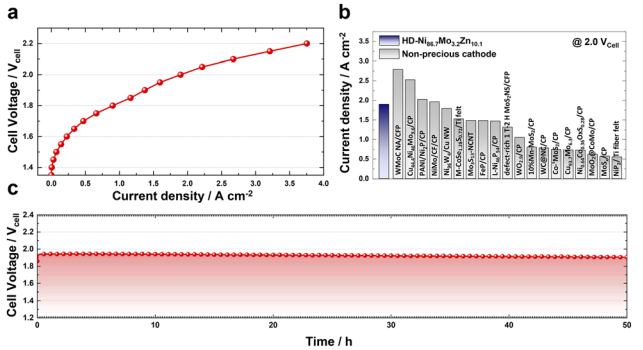


Fig. 4 (a) Single-cell polarization curve recorded using the HD-$Ni_{86.7}Mo_{3.2}Zn_{10.1}$ cathode. (b) Performance of HD$Ni_{86.7}Mo_{3.2}Zn_{10.1}$ and reported nonprecious cathodes compared by current density at 2.0 V_{cell}. (c) Long-term durability measurements performed at 1 A cm^{-2} for 50 h.

Fig. 3g shows the durability evaluation results for HD-$Ni_{86.7}Mo_{3.2}Zn_{10.1}$ under constant current of −10 mA cm^{-2} for 100 h. Over the 100 h test, the overpotential increased from 17 to 51 mV, indicating reasonable operation stability under acidic HER conditions. After 100 h, EDS shows Ni and Zn decreased by 0.8 at% and 1.5 at%, while Mo increased by 3.3 at%, indicating compositional redistribution. The loss of residual Ni and Zn with the surface reconstruction likely disrupts the defect-rich Ni-Mo framework, while severe coarsening (Fig. S5) degrades interfacial properties, leading to the increased HER overpotential. This finding suggests that further optimization may enhance long-term durability.

HD-$Ni_{86.7}Mo_{3.2}Zn_{10.1}$, which showed the best half-cell performance and stability, was further evaluated as the cathode in a PEMWE single cell. The membrane electrode assembly (MEA) was assembled with spray-coated IrO_2 on carbon paper as the anode and a Nafion 212 membrane. As shown in Fig. 4a, the single cell achieved a high performance of 1.897 A cm^{-2} at 2.0 V_{cell}, comparable to or exceeding previously reported nonprecious metal cathodes (Fig. 4b and Table S4). In addition, HD-$Ni_{86.7}Mo_{3.2}Zn_{10.1}$ exhibited a minimal difference of 0.155 A cm^{-2} at 2.0 V_{cell} compared to commercial Pt/C, highlighting its potential for practical application (Table S2). Furthermore, Fig. 4c shows the durability evaluation conducted at 1 A cm^{-2} for 50 h. HD-$Ni_{86.7}Mo_{3.2}Zn_{10.1}$ exhibited an extremely low deterioration rate of 0.9 mV h^{-1}, demonstrating excellent long-term stability under acidic PEMWE operating conditions.

In summary, we developed a high-performance, acid-durable NiMo-based cathode for PEMWE *via* selective Zn dealloying from a ternary NiMoZn alloy followed by annealing. While dealloying enhanced ECSA, annealing was crucial for structural stability against corrosion. The optimized catalyst showed an ultralow overpotential of 15.7 mV at −10 mA cm^{-2} and stable PEMWE single cell operation (1.897 A cm^{-2} at 2.0 V_{cell}). This study provides a practical strategy for designing robust nonprecious catalysts for water electrolysis.

Conflicts of interest

There are no conflicts to declare.

Data availability

The data supporting the findings of this study are available within the article and its supplementary information (SI). See DOI: https://doi.org/10.1039/d6cc00986g.

Acknowledgements

This study was supported by the National Research Foundation of Korea grant funded by the Korea government (MSIT) (RS-2024-00409901 and RS-2023-00235596).

References

1 T. M. Gür, Review of electrical energy storage technologies, materials and systems: challenges and prospects for large-scale grid storage, *Energy Environ. Sci.*, 2018, **11**(10), 2696–2767.
2 J. Turner, G. Sverdrup, M. K. Mann, P.-C. Maness, B. Kroposki, M. Ghirardi, R. J. Evans and D. Blake, Renewable hydrogen production, *Int. J. Energy Res.*, 2008, **32**(5), 379–407.
3 M. Ball and M. Wietschel, The future of hydrogen–opportunities and challenges, *Int. J. Hydrogen Energy*, 2009, **34**(2), 615–627.
4 M. Bonanno, K. Müller, B. Bensmann, R. Hanke-Rauschenbach, D. Aili, T. Franken, A. Chromik, R. Peach, A. T. Freiberg and S. Thiele, Review and prospects of PEM water electrolysis at elevated temperature operation, *Adv. Mater. Technol.*, 2024, **9**(2), 2300281.
5 T. Lim and S.-K. Kim, Non-precious hydrogen evolution reaction catalysts: Stepping forward to practical polymer electrolyte membrane-based zero-gap water electrolyzers, *Chem. Eng. J.*, 2022, **433**, 133681.
6 Y. Da, R. Jiang, Z. Tian, G. Chen, Y. Xiao, J. Zhang, S. Xi, Y. Deng, W. Chen, X. Han and W Hu, Development of a novel Pt_3V alloy electrocatalyst for highly efficient and durable industrial hydrogen evolution reaction in acid environment, *Adv. Energy Mater.*, 2023, **13**(16), 2300127.
7 P. Kuang, Z. Ni, B. Zhu, Y. Lin and J. Yu, Modulating the d-band center enables ultrafine Pt_3Fe alloy nanoparticles for pH-universal hydrogen evolution reaction, *Adv. Mater.*, 2023, **35**(41), 2303030.
8 Y. Shi, Z.-R. Ma, Y.-Y. Xiao, Y.-C. Yin, W.-M. Huang, Z.-C. Huang, Y.-Z. Zheng, F.-Y. Mu, R. Huang, G.-Y. Shi, Y.-Y. Sun, X.-H. Xia and W. Chen, Electronic metal–support interaction modulates single-atom platinum catalysis for hydrogen evolution reaction, *Nat. Commun.*, 2021, **12**(1), 3021.
9 K.-R. Yeo, H. Kim, K.-S. Lee, S. Kim, J. Lee, H. Park and S.-K. Kim, Controlled doping of ultralow amounts Ru on Ni cathode for PEMWE: Experimental and theoretical elucidation of enhanced performance, *Appl. Catal., B*, 2024, **346**, 123738.
10 D. Bernsmeier, M. Bernicke, E. Ortel, R. Schmack, J. Polte and R. Kraehnert, Soft-templated mesoporous RuPt/C coatings with enhanced activity in the hydrogen evolution reaction, *J. Catal.*, 2017, **355**, 110–119.
11 K. J. Choi and S.-K. Kim, A Pt cathode with high mass activity for proton exchange membrane water electrolysis, *Int. J. Hydrogen Energy*, 2023, **48**(3), 849–863.
12 S. Chatterjee, X. Peng, S. Intikhab, G. Zeng, N. N. Kariuki, D. J. Myers, N. Danilovic and J. Snyder, Nanoporous iridium nanosheets for polymer electrolyte membrane electrolysis, *Adv. Energy Mater.*, 2021, **11**(34), 2101438.
13 K.-R. Yeo, K.-S. Lee, H. Kim, J. Lee and S.-K. Kim, A highly active and stable 3D dandelion spore-structured self-supporting Ir-based electrocatalyst for proton exchange membrane water electrolysis fabricated using structural reconstruction, *Energy Environ. Sci.*, 2022, **15**(8), 3449–3461.
14 S. Anantharaj and S. Noda, Electrochemical dealloying-assisted activity enhancement: The next big thing in water electrosplitting!, *Nano Energy*, 2023, **114**, 108624.
15 H. M. C. M. Jayawardana, S. Meng, B. A. Yusuf, J. Jing, H. Ren, Q. Nie, J. Xie, M. Chen and Y. Xu, Synergistic flower-like N-doped Co/Mo_2C catalyst for hydrogen evolution reaction in universal pH and high-performance alkaline water-splitting, *Mater. Today Chem.*, 2025, **43**, 102476.

Open Access Article. Published on 17 April 2026. Downloaded on 4/28/2026 2:08:19 AM.
This article is licensed under a Creative Commons Attribution-NonCommercial 3.0 Unported Licence.

16 H. Kim, H. Park, D.-K. Kim, S. Oh, I. Choi and S.-K. Kim, Electrochemically fabricated NiW on a Cu nanowire as a highly porous non-precious-metal cathode catalyst for a proton exchange membrane water electrolyzer, *ACS Sustainable Chem. Eng.*, 2019, **7**(9), 8265–8273.
17 K. J. Choi, H. Kim and S.-K. Kim, Multicomponent nonprecious hydrogen evolution catalysts for high performance and durable proton exchange membrane water electrolyzer, *J. Power Sources*, 2021, **506**, 230200.
18 X. Wang, R. Su, H. Aslan, J. Kibsgaard, S. Wendt, L. Meng, M. Dong, Y. Huang and F. Besenbacher, Tweaking the composition of NiMoZn alloy electrocatalyst for enhanced hydrogen evolution reaction performance, *Nano Energy*, 2015, **12**, 9–18.
19 Y. Mo, Y. Ni, X. Li, R. Pan, Y. Tang, Y. Deng, B. Xiao, Y. Tan and F. Yu, An efficient pH-universal non-noble hydrogen-evolving electrocatalyst from transition metal phosphides-based heterostructures, *Int. J. Hydrogen Energy*, 2023, **48**(80), 31101–31109.
20 W. K. Zhao, Z. Q. Ma, J. Y. Zheng, C. B. Han, K. L. Zhou, M. Y. Hao, D. C. Fang, Y. Xia and H. Yan, Dual-functional MnS_2/MnO_2 heterostructure catalyst for efficient acidic hydrogen evolution reaction and assisted degradation of organic wastewater, *J. Energy Chem.*, 2023, **87**, 215–224.
21 C. H. Lee, K.-R. Yeo and S.-K. Kim, Highly Active and Durable NiMoMn Hydrogen Evolution Catalysts for Proton-Exchange Membrane Water Electrolysis, *Int. J. Energy Res.*, 2025, 5812374.
22 H. S. Park, K.-R. Yeo, W. S. Jung and S.-K. Kim, Electrodeposited ternary CuNiMo catalysts for alkaline hydrogen oxidation, *Electron. Mater. Lett.*, 2024, **20**(3), 293–305.
23 M. Donten, H. Cesiulis and Z. Stojek, Electrodeposition of amorphous/nanocrystalline and polycrystalline Ni–Mo alloys from pyrophosphate baths, *Electrochim. Acta*, 2005, **50**(6), 1405–1412.
24 Z. Wang, X. Ge, Z. Li, J. Wu, Z. Liang and S. Wang, Mo-doped NiCu as an efficient and stable electrocatalyst for the hydrogen evolution reaction, *New J. Chem.*, 2019, **43**(24), 9652–9657.
25 M. Nagoshi and A. Miyamoto, Electronic Structure of Electrodeposited Zn-Ni Alloy Coating Studied by UPS and XPS, *Hyomen Kagaku*, 1996, **17**(5), 282–285.
26 Y. Yu, W. Xiao, J. Wang and L. Wang, Understanding the surface segregation behavior of transition metals on Ni (111): a first-principles study, *Phys. Chem. Chem. Phys.*, 2016, **18**(38), 26616–26622.
27 L. Wang, Y. Lin, Z. Zeng, W. Liu, Q. Xue, L. Hu and J. Zhang, Electrochemical corrosion behavior of nanocrystalline Co coatings explained by higher grain boundary density, *Electrochim. Acta*, 2007, **52**(13), 4342–4350.